Physical and Engineering Sciences in Medicine (2023) 46:1713–1721
https://doi.org/10.1007/s13246-023-01331-7

SCIENTIFIC PAPER

Physical characteristics of deep learning-based image processing software in computed tomography: a phantom study

Seiya Sato[1] · Atsushi Urikura[1] · Makoto Mimatsu[1] · Yuta Miyamae[1] · Yuji Jibiki[2] · Mami Yamashita[2] · Toshihiro Ishihara[1]

Received: 4 September 2022 / Accepted: 6 September 2023 / Published online: 19 September 2023

Abstract

Purpose This study aimed to assess the image characteristics of deep-learning-based image processing software (DLIP; FCT PixelShine, FUJIFILM, Tokyo, Japan) and compare it with filtered back projection (FBP), model-based iterative reconstruction (MBIR), and deep-learning-based reconstruction (DLR).

Methods This phantom study assessed the object-specific spatial resolution (task-based transfer function [TTF]), noise characteristics (noise power spectrum [NPS]), and low-contrast detectability (low-contrast object-specific contrast-to-noise ratio [CNR_{LO}]) at three different output doses (standard: 10 mGy; low: 3.9 mGy; ultralow: 2.0 mGy). The processing strength of $DLIP_{FBP}$ with A1, A4, and A9 was compared with those of FBP, MBIR, and DLR.

Result The standard dose with high-contrast TTFs of $DLIP_{FBP}$ exceeded that of FBP. Low-contrast TTFs were comparable to or lower than that of FBP. The NPS peak frequency (f_P) of $DLIP_{FBP}$ shifts to low spatial frequencies of up to 8.6% at ultralow doses compared to the standard FBP dose. MBIR shifted the most f_P compared to FBP—a marked shift of up to 49%. $DLIP_{FBP}$ showed a CNR_{LO} equal to or greater than that of DLR in standard or low doses. In contrast, the CNR_{LO} of the $DLIP_{FBP}$ was equal to or lower than that of the DLR in ultralow doses.

Conclusion $DLIP_{FBP}$ reduced image noise while maintaining a resolution similar to commercially available MBIR and DLR. The slight spatial frequency shift of f_P in $DLIP_{FBP}$ contributed to the noise texture degradation suppression. The NPS suppression in the low spatial frequency range effectively improved the low-contrast detectability.

Keywords Deep-learning image processing · Denoising · Computed tomography · NPS · TTF · CNR

Introduction

Owing to the increasing number of computed tomography (CT) units in each country and number of CT scans per unit population, reducing the radiation dose patients receive from these examinations is particularly important [1, 2]. However, reducing the radiation dose would reduce the number of photons reaching the detector, increase image noise, and consequently affect the diagnostic performance of CT [3, 4]. Manufacturers have implemented many dose reduction techniques and solutions to curb the high exposure in CT [5, 6]. For example, iterative reconstruction (IR) was developed to reduce the image noise while maintaining the spatial resolution and contrast-to-noise ratio (CNR) [7–9].

IR is a statistical or algebraic reconstruction algorithm [10]. Model-based IR [MBIR] that modeled the object as well as the noise and scanner system in the projection data. Detailed principles of MBIR have been reported in previous studies [10, 11]. The data fidelity of MBIR is based on a forward projection model that models scanner geometry, optics, and statistical noise characteristics [12]. However, the commercial implementation of IR is not adopted by all medical institutions because it depends on the vendor and CT scanner generation. Additionally, MBIR remained installed on only a few machines.

Several third-party manufacturers released an image-based universal IR system (image-based IR) that achieves

✉ Atsushi Urikura
aurikura@ncc.go.jp

[1] Department of Radiological Technology, Radiological Diagnosis, National Cancer Center Hospital, 5-1-1 Tsukiji, Chuo-Ku, Tokyo 104-0045, Japan

[2] Clinical Product Specialist Marketing Group, FUJIFILM Corporation, 7-3, Akasaka 9-Chome Minato-Ku, Tokyo, Japan

denoising by processing already reconstructed FBP images [13–15]. Image-based IR is a versatile technology that is independent of CT systems and vendors. Previous studies have shown that the image characteristics are comparable to hybrid IR in low-dose CT. A new deep learning-based universal image processing software (DLIP; FCT PixelShine, FUJIFILM, Tokyo, Japan) is an image processing technique trained by deep learning to improve the image quality in low-dose CT. DLIP is as universal as image-based IR and is expected to denoise with natural textures because of deep-learning techniques. The DLIP uses deep learning techniques and ultralarge amounts of training pairs of noisy low- and high-dose images [16] and performs noise reduction on any input image regardless of the CT manufacturer. Other DLRs, such as AiCE and TrueFidelity (GE Healthcare, Waukesha, WI, USA) are noise reduction algorithms that respond to vendor-specific input images [17, 18]. DLIP software can be used by installing it on a three-dimensional image analysis workstation. It can be retrospectively applied to images reconstructed using any algorithm (filtered back projection: FBP, IR, and DLR). To the best of our knowledge, no study has assessed the detailed image characteristics of DLIP.

Therefore, this study aimed to assess the image characteristics of DLIP and compare them with FBP, MBIR, and deep-learning-based reconstruction (DLR).

Methods

Phantoms

The American College of Radiology (ACR) phantom (model 464, Gammex, Middleton Wi, USA) was placed at the center of gantry rotation to measure the object-specific spatial resolution. The ACR phantom is 200 mm in diameter, and four different test object rods (bone, water, polyethylene, and acrylic) were embedded. Catphan 500 phantom (Phantom Laboratory, Salem NY, USA) with a uniform module (CTP 486) and low-contrast module (CTP 515) was used to measure the image noise and low-contrast detectability.

Data acquisition and image reconstruction

An ultrahigh resolution CT scanner (Aquilion Precision, Canon Medical Systems, Tochigi, Japan) was used to acquire all data. Three different output dose (volume CT dose index [$CTDI_{vol}$]) settings were determined as 10.0, 3.9, and 2.0 mGy for assessing the image characteristics corresponding to the image noise level. Thus, size-specific dose estimate according to the conversion formula from $CTDI_{vol}$ reported by the American Association of Physicists in Medicine Task Group 220 [19] were 17.8, 6.9, and 3.6 mGy, respectively (conversion factor of 200 mm effective diameter of 1.78). These are referred to as standard, low, and ultralow. Other acquisition parameters were as follows: a tube voltage of 120 kV, rotation time of 0.5 s, detector configuration of 160 × 0.25 mm, a pitch factor of 0.81, thickness of 0.25 mm, and an X-ray focus size of 0.6 × 0.6 mm. The field of view (FOV) was determined at 350 mm with 1024 × 1024 matrix. All images were reconstructed with FBP (FC13; standard soft kernel), MBIR (forward projected model-based Iterative Reconstruction Solution: FIRST BODY standard), and DLR (Advanced Intelligent Clear-IQ Engine: AiCE BODY Standard). Moreover, FBP images were postprocessed with acquired DLIP ($DLIP_{FBP}$) The DLIP has variable processing strengths from A1 to A9 [20]. Here, "A" denotes "adaptive" and indicates a function of noise reduction strength, and $DLIP_{FBP}$ strengths of 1, 4, and 9 were used in this study. It should be noted that the DLIP software used here was a prototype.

Object-specific spatial resolution

The task-based transfer function (TTF) was calculated to measure the object-specific spatial resolution corresponding to the contrast and image noise. A circular edge method was performed to acquire the TTF [21]. Two test rods were used with a CT number of approximately 955 HU (bone equivalent; high contrast) and 120 HU (acrylic; soft tissue contrast). Phantom images were prepared by subtracting the start image from the end image to perform an accurate alignment in a longitudinal direction, and it was confirmed without misregistration. To ensure the accuracy of radial profile measurements, an accurate alignment is important for the circular edge method. A region of interest (ROI) was placed around the test rod as shown in Fig. 1. Radial profiles from the center coordinates of the square ROI were automatically acquired. A one-dimensional edge spread function from radial edges across a test rod was synthesized and differentiated to obtain a line spread function. A total of 600 images (60 consecutive images × 10 times repeated acquisition) were acquired per scanning condition were acquired. These 600 images were processed, and an averaged image for each condition was measured [22]. TTF was measured for bone and acrylic material using CTmeasure software [23].

Noise characteristics

The CTP 486 module (uniformity section of CATPHAN) was scanned to analyze the noise characteristics corresponding to the spatial frequency, and the noise power spectrum (NPS) was calculated. A 128 × 128 square ROI was placed at the center of the acquired phantom images. The NPS was calculated using two-dimensional Fourier transform. Each dataset contained 60 consecutive uniform axial images

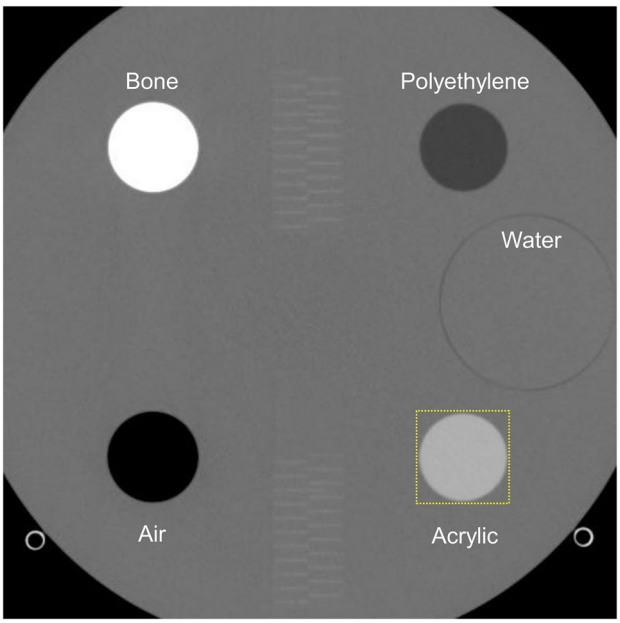

Fig. 1 Schema of the phantom image to perform the circular edge method. A region of interest (ROI) was arranged to acquire the edges of each rod. (Figure shows an ROI placed on an acrylic rod.)

within the CTP486 module. The NPS was averaged from 60 images for each dataset. The peak (f_P; cycles/mm) and average (f_A; cycles/mm) frequencies were calculated [24].

Low-contrast detectability

Low-contrast detectability was evaluated with the CTP515 module (low-contrast detectability section of Catphan) using a low-contrast object-specific contrast-to-noise ratio (CNR_{LO}) as an index that reflects the contrast of the lesion, noise characteristics, and the frequency components corresponding to the lesion size [25]. The CNR_{LO} could be calculated from the following equation, which incorporates the NPS:

$$CNR_{LO} = \frac{ROI_M - ROI_B}{\sqrt{NPS(\bar{u})}}, \quad (1)$$

where, ROI_M and ROI_B are CT values measured at the lesion and background ROI, respectively, and NPS ($\bar{u}$) is the NPS at the spatial frequency ($\bar{u}$). NPS ($\bar{u}$) represents the amount of noise at the spatial frequency that involves target lesion detection. The low-contrast signal (placed at ROI_M) has a nominal contrast of 10 HU with a 5-mm diameter (Fig. 2). $\bar{u}$ represents the spatial frequency that contributes most to detectability corresponding to the target lesion diameter. Then, NPS ($\bar{u}$) was calculated with a spatial frequency of 0.105 cycles/mm obtained from the above section.

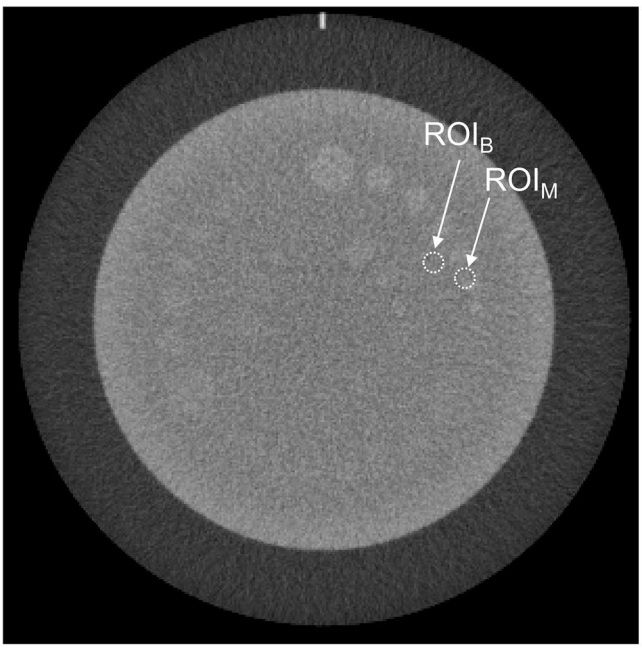

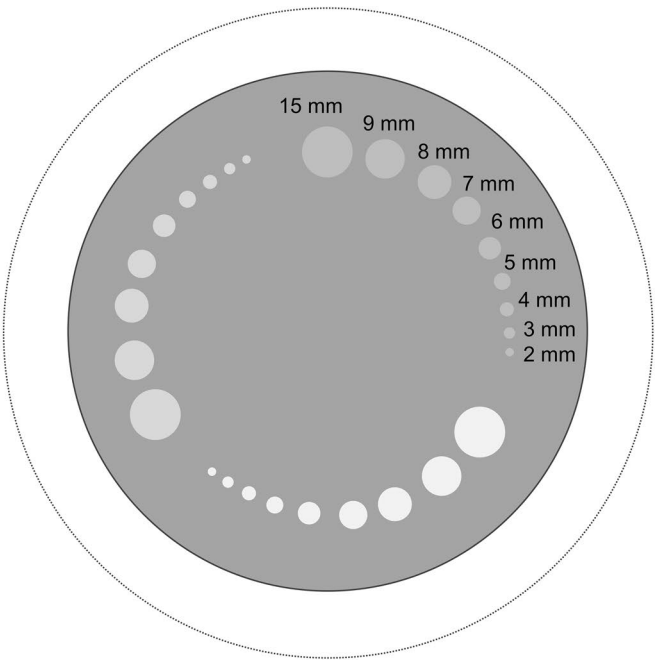

Fig. 2 The low-contrast module (CTP 515) in Catphan phantom was used for measuring the low-contrast object-specific contrast-to-noise ratio. A low-contrast signal used in this study has a nominal contrast of ~ 10 HU (contrast level of 1.0%). The ROIs were placed at a 5 mm diameter object (ROI_M) and background (ROI_B)

Subtraction image measurement for structural changes

Structural changes between the FBP and the corresponding $DLIP_{FBP}$ were determined by subtracting the two images. Acquired ACR phantom images at the same slice location were subtracted between FBP and $DLIP_{FBP}$ images of A1, A4, and A9, respectively. Subtraction images were calculated from images scanned under low-dose conditions (3.9 mGy of $CTDI_{vol}$). The area of interest of 400 mm^2 (20 × 20 mm square) was placed at the four test rod materials (bone, air, polyethylene, and acrylic) enclosed in the ACR phantom to evaluate the slight change in CT value between FBP and $DLIP_{FBP}$, and the CT value was measured. CT values were measured on 10 consecutive subtraction slices at each DLIP strength.

Typical image processing run time

To compare the run time for image reconstruction or processing, the times were measured for FBP, MBIR, DLR, and $DLIP_{FBP}$. The time was measured with a slice thickness of 0.25 mm and FOV of 350 mm with 1,024 × 1,024 matrix. The run time of image processing was measured for 1000 images for each reconstruction obtained by scanning with Catphan phantom. Time measurements were performed thrice for each method. The time of $DLIP_{FBP}$ indicates the postprocessing only, and additional time is required to perform FBP reconstruction at a scanner console and transfer it to a workstation.

Results

Object-specific spatial resolution

Figure 3 shows the TTF calculated using three different algorithms for high- and low-contrast objects. Tables 1 and 2 summarizes the value of 50% TTF and 10% TTF. High-contrast TTFs with the standard dose of all reconstruction algorithms exceeded that of FBP, with MBIR exhibiting the highest value. In particular, the 10% TTF of $DLIP_{FBP}$ was improved by up to 71% compared to FBP under the ultralow-dose condition. Low-contrast TTFs were comparable to or lower than that of FBP for all doses.

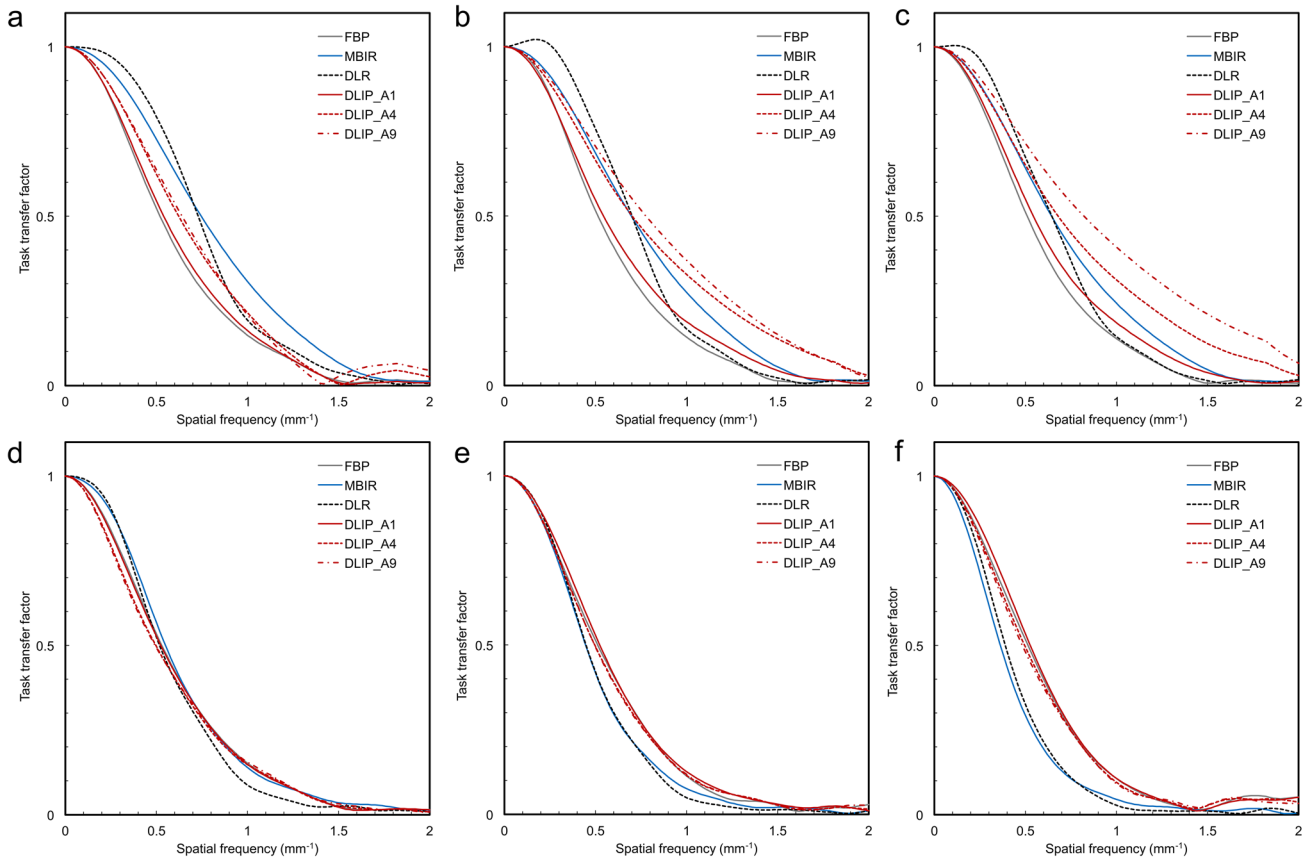

Fig. 3 Task transfer function (TTF) for high- and low-contrast objects (upper and lower column) with standard (**a**, **d**), low (**b**, **e**), and ultralow (**c**, **f**) doses, respectively. The TTF shows different trends depending on radiation dose and image reconstruction algorithms

Noise characteristics

Figure 4 shows the NPS results, and Tables 3 and 4 shows the f_P and f_A for each reconstruction algorithm. Conspicuous rise-up of NPS curve were observed at low spatial frequencies of < 0.1 mm^{-1} with $DLIP_{FBP}$ in low- and ultralow-dose. It was thought to be due to the increase in noise from streak artifacts corresponding to dose reduction as described in

Table 1 Task transfer function with high- and low-contrast objects for FBP, MBIR, and DLR

	50% TTF, cycles/mm			10% TTF, cycles/mm		
	FBP	MBIR	DLR	FBP	MBIR	DLR
High contrast						
Standard	0.52	0.74	0.71	1.15	1.41	1.26
Low	0.51	0.7	0.7	1.12	1.36	1.18
Ultra-low	0.51	0.64	0.64	1.11	1.32	1.12
Low contrast						
Standard	0.53	0.53	0.52	1.16	1.12	0.95
Low	0.51	0.44	0.45	1.01	0.92	0.88
Ultra-low	0.51	0.36	0.39	1.02	0.76	0.77

TTF task transfer function, *FBP* filtered back projection, *MBIR* model-based iterative reconstruction, *DLR* deep learning-based reconstruction

Table 2 Task transfer function with high- and low-contrast objects for $DLIP_{FBP}$

	50% TTF, cycles/mm			10% TTF, cycles/mm		
	$DLIP_{FBP}$			$DLIP_{FBP}$		
	A1	A4	A9	A1	A4	A9
High contrast						
Standard	0.54	0.62	0.64	1.17	1.22	1.19
Low	0.54	0.7	0.77	1.28	1.63	1.67
Ultra-low	0.54	0.68	0.82	1.24	1.6	1.9
Low contrast						
Standard	0.52	0.5	0.49	1.15	1.17	1.18
Low	0.52	0.5	0.49	1.08	1.04	1.05
Ultra-low	0.53	0.5	0.48	1.02	0.97	0.98

TTF task transfer function, A1, A4, and A9 were the processing strengths of a deep learning-based universal image processing software (FCT PixelShine, FUJIFILM, Tokyo, Japan)

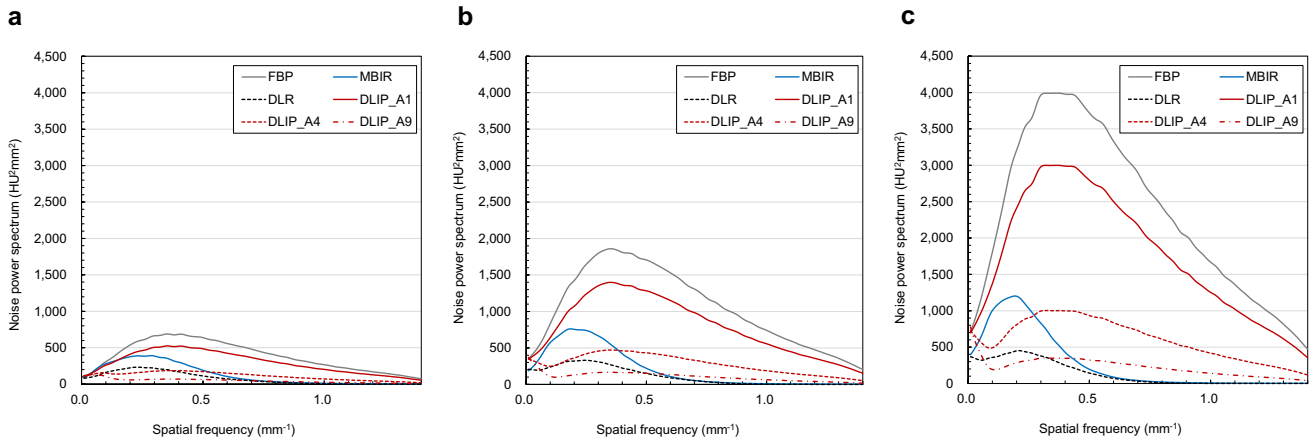

Fig. 4 Noise power spectrum (NPS) obtained by standard (**a**), low (**b**), and ultralow (**c**) dose settings. The height of the NPS curve with A4 and A9 showed lower than the standard DLR dose, and A4 showed higher than that of low and ultralow DLR doses

Table 3 Peak and average spatial frequency of noise power spectrum obtained from three different dose levels with FBP, MBIR, and DLR

$CTDI_{vol}$ (mGy)	Peak spatial frequency (f_P; mm^{-1})			Average spatial frequency (f_A; mm^{-1})		
	FBP	MBIR	DLR	FBP	MBIR	DLR
Standard (10.0)	0.35	0.29	0.23	0.58	0.34	0.34
Low (3.9)	0.35	0.18	0.24	0.58	0.29	0.31
Ultra-low (2.0)	0.37	0.19	0.21	0.58	0.25	0.27

$CTDI_{vol}$ volume computed tomography dose index, *FBP* filtered back projection, *MBIR* model-based iterative reconstruction, *DLR* deep learning-based reconstruction

Table 4 Peak and average spatial frequency of noise power spectrum obtained from three different dose levels with $DLIP_{FBP}$

$CTDI_{vol}$ (mGy)	Peak spatial frequency (f_P; mm^{-1})			Average spatial frequency (f_A; mm^{-1})		
	$DLIP_{FBP}$			$DLIP_{FBP}$		
	A1	A4	A9	A1	A4	A9
Standard (10.0)	0.35	0.35	0.35	0.57	0.54	0.48
Low (3.9)	0.35	0.35	0.35	0.58	0.56	0.51
Ultra-low (2.0)	0.37	0.32	0.32	0.58	0.56	0.52

$CTDI_{vol}$ volume computed tomography dose index, A1, A4, and A9 were the processing strengths of a deep learning-based universal image processing software (FCT PixelShine, FUJIFILM, Tokyo, Japan)

previous study [26]. Therefore, we recorded the f_P value for $DLIP_{FBP}$ at the region of spatial frequency excluding rise-up. The f_P and f_A for $DLIP_{FBP}$ exhibited a slight shift in spatial frequency. $DLIP_{FBP}$ minimized the f_P shift under all dose conditions; f_P shifts toward lower spatial frequency were indicated up to 8.6% with an ultralow dose compared to the standard FBP dose. Most MBIR shifted in f_P compared with FBP, with marked shifts of up to 49%. A structural change in the image texture is shown by the spatial frequency shift of f_P and f_A.

Low-contrast detectability

Figure 5 shows the CNR_{LO} for each reconstruction algorithm acquired from different dose levels. The CNR_{LO} improved in $DLIP_{FBP}$ depending on the dose and strength. Overall, MBIR, DLR, and $DLIP_{FBP}$ outperformed FBP in the same dose levels. A1 strength $DLIP_{FBP}$ showed a CNR_{LO} equal to DLR in standard or low doses, whereas CNR_{LO} of A4 and A9 strength $DLIP_{FBP}$ was greater than DLR. In contrast, the A1 and A4 strength of $DLIP_{FBP}$ indicated a CNR_{LO} equal to or less than that of the DLR in ultralow doses.

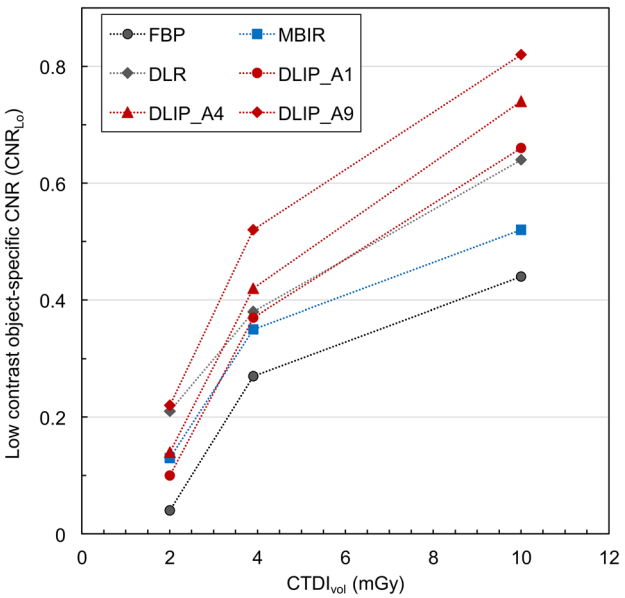

Fig. 5 A plot of CNR_{LO} acquired with each reconstruction algorithm. MBIR, DLR, and $DLIP_{FBP}$ outperformed FBP at the same dose levels investigated

Subtraction image measurement for structural changes

Figure 6 shows the images with FBP, $DLIP_{FBP}$ with three strength settings, and the corresponding subtraction. The obtained subtraction image from A1 showed no edge structure but only noise. Conversely, the subtraction images of A4 and A9 showed edge structures at the rods and phantom boundaries. Additionally, a slight change in CT value was observed for the two lower attenuation test rods (polyethylene and acrylic). The fluctuation of CT value measured by the subtraction image occurred in two rods with low attenuation according to the $DLIP_{FBP}$ strength, as shown in Fig. 7. Changes in CT values of the two rods

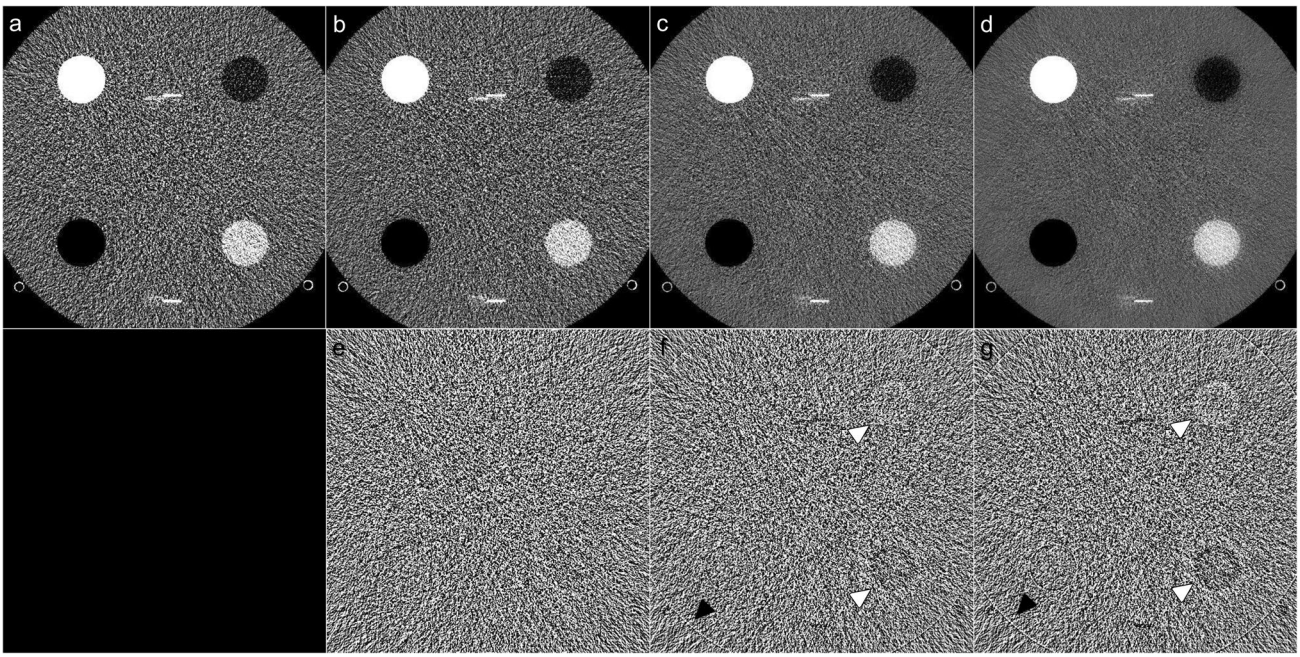

Fig. 6 Images with FBP (**a**), $DLIP_{FBP}$-A1 (**b**), -A4 (**c**), -A9 (**d**), and the corresponding subtracted images (**e**–**g**). The subtracted image of A1 showed no edge structure (**e**), and A4 and A9 (**f**, **g**) showed the edge and rod structure (black and white arrowhead). All images were displayed with a window level and width of 50 HU and 300 HU, respectively

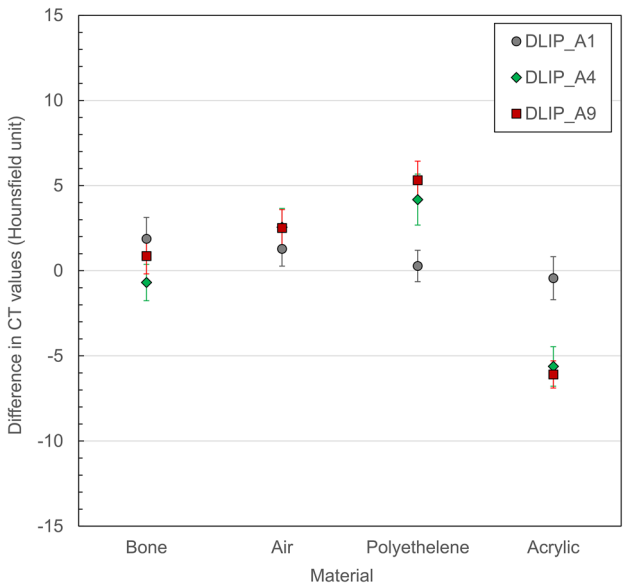

Fig. 7 Fluctuation of CT value measured by the subtraction images. The CT values of polyethylene and acrylic rods indicate a slight fluctuation and contrast degradation

exhibited a slight degradation in contrast. Contrast reduction was dependent on DLIP strength, with a maximum of 5.3 and 6.1 HU for polyethylene and acrylic, respectively.

Typical run time of image processing

The mean reconstruction or processing times and their standard deviations for FBP, MBIR, DLR, and $DLIP_{FBP}$ were 30 s ± 1 s, 19 min 47 ± 6 s, 2 min 33 ± 1 s, and 2 min 32 ± 6 s, respectively, where the time of $DLIP_{FBP}$ is for postprocessing only. Additional time is required to perform FBP reconstruction at a scanner console and transfer it to a workstation.

Discussion

To the best of our knowledge, this study is the first detailed assessment of the physical characteristics of a prototype DLIP software, FCT PixelShine. $DLIP_{FBP}$ may show image quality improvements comparable to commercially available DLRs.

The TTF of $DLIP_{FBP}$ showed different values depending on the radiation dose and contrast of the object. Nonlinear algorithms, such as MBIR and DLR, are known to exhibit different spatial resolution characteristics depending on the amount of noise and contrast [27, 28], and the object-specific task-based spatial resolution characteristics of $DLIP_{FBP}$ are similar to those of existing nonlinear algorithms. However, the 10% TTF of $DLIP_{FBP}$ corresponding to low-contrast objects was comparable to that of DBP and

MBIR in standard dose acquisition; it indicated a higher value than that of MBIR and DLR in low- and ultra-low-dose acquisitions.

The NPS curve exhibited a dose-specific trend as shown in Fig. 4. The peaks of NPS curves with strengths A4 and A9 were lower than those of DLR at standard dose. Conversely, A4 was higher than that of DLR at low and ultralow doses. The f_P or f_A shift varied with dose and reconstruction algorithm and processing strength. f_A shifts were up to 1.7%, 6.9%, 17.2%, 56.9%, and 53.4% for A1, A4, A9, MBIR, and DLR, respectively. The spatial frequency shift in f_A would cause image texture changes relative to FBP. $DLIP_{FBP}$ exhibited significantly less spatial frequency shift compared to MBIR and DLR, indicating the possibility of obtaining images with noise texture close to FBP. However, the evaluated DLR was an algorithm developed using the precise MBIR quality as a supervised image [29]. The f_A shift of DLR to standard-dose MBIR was up to 20.6%, which should be compared with MBIR rather than with FBP.

CNR_{LO} indicated as an index of low-contrast detectability for 5 mm diameter lesions. The low-contrast detectability of $DLIP_{FBP}$ was comparable to or better than that of DLR at standard and low doses, but it was comparable to or lower than that of DLR at ultralow doses. CNR_{LO} is an index that reflects the noise power value at the spatial frequency corresponding to the lesion diameter. Therefore, the detectability of $DLIP_{FBP}$ was improved compared to that of conventional FBP. In particular, the acquired A4 and A9 detectability at low dose was comparable to that of FBP at a standard dose.

The edge signals observed in the subtraction images posed a problem in noise reduction and maintaining image quality for tissue and structure boundaries. The higher strength of $DLIP_{FBP}$ at low doses may impair the image quality for diagnosis. Although the low-strength $DLIP_{FBP}$ image did not depict the edge signal, there was a limited noise reduction. Signal value measurements of subtraction images revealed that $DLIP_{FBP}$ slightly reduced the contrast of low attenuation objects. This tendency appeared at a low dose and higher strength settings in particular. The effect on clinical imaging is a topic for future study.

Our study has several limitations. First, this study conducted phantom studies with only limited tasks (e.g., image noise, object diameter, contrast, and lesion diameter). We have not assessed the effect of complex anatomy or patient diameter on image quality in vivo. Thus, in vivo clinical evaluation needs to be conducted in the future. Secondly, $DLIP_{FBP}$ was applied only to FBP images in this study although DLIP is applicable to all CT images, including MBIR or DLR images. If the other reconstruction is obtained and applied to DLIP, it may show a different noise texture. Third, the determined slice thickness, matrix, and FOV for the phantom acquisitions were limited. Measurements with thicker slice thicknesses and/or fewer pixels may be necessary. Fourth, a subjective observer test would be necessary to confirm the $DLIP_{FBP}$ performance. The quantitative evaluation results in this study would be provided as one of the pieces of evidence for those findings. Fifth, this study did not include the evaluation of artifacts because of low dose acquisition. At least, we did not observe any specific artifacts during the phantom experiments. However, the evaluation of artifacts may be required in the future. Finally, the $DLIP_{FBP}$ used herein was a prototype; hence, the results might differ from those obtained using commercial versions of the software.

Conclusion

A prototype $DLIP_{FBP}$ reduced the image noise while maintaining the resolution for high-contrast objects similar to commercially available MBIR and DLR. The significantly reduced spatial frequency shift of f_A in $DLIP_{FBP}$ compared to that in MBIR and DLR contributed to the suppression of noise texture changes. The NPS suppression in the low-spatial frequency range effectively improved the low-contrast detectability of $DLIP_{FBP}$ compared to that of FBP. Evaluating the $DLIP_{FBP}$ performance in vivo is a subject for future work.

Acknowledgements This study was supported as a joint research project by FUJIFILM Corporation. A.U. is currently receiving a grant (JSPS KAKENHI Grant No. 22K15834). The authors are grateful to the radiological diagnosis staff of the National Cancer Center Hospital who supported this study.

Author contributions All authors contributed to the study conception and design. Material preparation, data collection, and analysis were performed by SS, AU, and MM. The first draft of the manuscript was written by SS and AU and all authors commented on previous versions of the manuscript. All authors read and approved the final manuscript.

Funding This work was supported by FUJIFILM Corporation as a joint research project. Atsushi Urikura is currently receiving a grant (JSPS KAKENHI Grant No. 22K15834).

Data availability The data that support the findings of this study are available from the corresponding author, AU, upon reasonable srequest.

Declarations

Conflict of interest Yuji Jibiki and Mami Yamashita are employees of FUJIFILM Corporation. The authors have no relevant financial or non-financial interests to disclose.

Ethical approval This article does not contain any studies with human participants or animals performed by any of the authors.

References

1. Organisation for Economic Co-operation and Development (OECD). [Available from: https://data.oecd.org/healthcare/computed-tomography-ct-exams.htm]. Accessed 2 Aug 2023
2. Urikura A, Yoshida T, Matsubara K, Nomura K, Hoshino T, Takagi T (2023) Number of computed tomography scanners and

regional disparities based on population and medical resources in Japan. Radiol Phys Technol. https://doi.org/10.1007/s12194-023-00725-2. (**Epub ahead of print**)
3. Goenka AH, Herts BR, Obuchowski NA, Primak AN, Dong F, Karim W et al (2014) Effect of reduced radiation exposure and iterative reconstruction on detection of low-contrast low-attenuation lesions in an anthropomorphic liver phantom: an 18-reader study. Radiology 272:154–163. https://doi.org/10.1148/radiol.14131928
4. Jensen CT, Wagner-Bartak NA, Vu LN, Liu X, Raval B, Martinez D et al (2019) Detection of colorectal hepatic metastases is superior at standard radiation dose CT versus reduced dose CT. Radiology 290:400–409. https://doi.org/10.1148/radiol.2018181657
5. Akai H, Kiryu S, Shibata E, Maeda E, Sato J, Tomizawa N et al (2016) Reducing CT radiation exposure with organ effective modulation: a retrospective clinical study. Eur J Radiol 85:1569–1573. https://doi.org/10.1016/j.ejrad.2016.06.008
6. Nam JG, Hong JH, Kim DS, Oh J, Goo JM (2021) Deep learning reconstruction for contrast-enhanced CT of the upper abdomen: similar image quality with lower radiation dose in direct comparison with iterative reconstruction. Eur Radiol 31:5533–5543. https://doi.org/10.1007/s00330-021-07712-4
7. Prakash P, Kalra MK, Kambadakone AK, Pien H, Hsieh J, Blake MA et al (2010) Reducing abdominal CT radiation dose with adaptive statistical iterative reconstruction technique. Investig radiol 45:202–210. https://doi.org/10.1097/RLI.ob013e3181dzfeec
8. Beister M, Kolditz D, Kalender WA (2012) Iterative reconstruction methods in X-ray CT. Phys Med 28:94–108. https://doi.org/10.1016/j.ejmp.2012.01.003
9. Desai G, Thabet A, Elias A, Sahani D (2013) Comparative assessment of three image reconstruction techniques for image quality and radiation dose in patients undergoing abdominopelvic multidetector CT examinations. Br J Radiol. https://doi.org/10.1259/bjr.20120161
10. Stiller W (2018) Basics of iterative reconstruction methods in computed tomography: a vendor-independent overview. Eur J Radiol 109:147–154. https://doi.org/10.1016/j.ejrad.2018.10.025
11. Mileto A, Guimaraes LS, McCollough CH, Fletcher JG, Yu L (2019) State of the art in abdominal CT: the limits of iterative reconstruction algorithms. Radiology 293:491–503. https://doi.org/10.1148/radiol.2019191422
12. Ohno Y, Yaguchi A, Okazaki T, Aoyagi K, Yamagata H, Sugihara N et al (2016) Comparative evaluation of newly developed model-based and commercially available hybrid-type iterative reconstruction methods and filter back projection method in terms of accuracy of computer-aided volumetry (CADv) for low-dose CT protocols in phantom study. Eur J Radiol 85:1375–1382. https://doi.org/10.1016/j.ejrad.2016.05.001
13. Pourjabbar S, Singh S, Kulkarni N, Muse V, Digumarthy SR, Khawaja RD et al (2015) Dose reduction for chest CT: comparison of two iterative reconstruction techniques. Acta Radiol 56:688–695. https://doi.org/10.1177/0284185114537256
14. Kawashima H, Ichikawa K, Matsubara K, Nagata H, Takata T, Kobayashi S (2019) Quality evaluation of image-based iterative reconstruction for CT: ccomparison with hybrid iterative reconstruction. J Appl Clin Medical Phys 20:199–205. https://doi.org/10.1002/acm2.12597
15. Watanabe S, Ichikawa K, Kawashima H, Kono Y, Kosaka H, Yamada K et al (2020) Image quality comparison of a nonlinear image-based noise reduction technique with a hybrid-type iterative reconstruction for pediatric computed tomography. Phys Med 76:100–108. https://doi.org/10.1016/j.ejmp.2020.06.015
16. Tian SF, Liu AL, Liu JH, Liu YJ, Pan JD (2019) Potential value of the PixelShine deep learning algorithm for increasing quality of 70 kVp+ASiR-V reconstruction pelvic arterial phase CT images. Jpn J Radiol 37:186–190. https://doi.org/10.1007/s11604-018-0798-0
17. Boedeker K (2019) AiCE deep learning reconstruction: bringing the power of ultra-high resolution CT to routine imaging. Canon Medical Systems Corporation. [Available from: https://es.medical.canon/wp-content/uploads/sites/20/2019/11/White-paper-Kirsten-Boedeker.pdf]. Accessed 2 Aug 2023
18. Hsieh J, Liu E, Nett B, Tang J, Thibault JB, Sahney S (2019) A new era of image reconstruction: TrueFidelity™. White Paper (JB68676XX), GE Healthcare. [Available from: https://www.gehealthcare.com.br/-/jssmedia/040dd213fa89463287155151fdb01922.pdf]. Accessed 2 Aug 2023
19. McCollough C, Bakalyar DM, Bostani M, Brady S, Boedeker K, Boone JM et al (2014) Use of water equivalent diameter for calculating patient size and size-specific dose estimates [SSDE] in CT: the Report of AAPM Task Group 220. AAPM Rep 2014:6–23
20. FUJIFILM. FCT PixelShine [Available from: https://asset.fujifilm.com/www/uk/files/2021-05/1f64fbb72811e1afea76c4fbc618bb19/Pixel_Shine.pdf]. Accessed 2 Aug 2023
21. Richard S, Husarik DB, Yadava G, Murphy SN, Samei E (2012) Towards task-based assessment of CT performance: system and object MTF across different reconstruction algorithms. Med Phys 39:4115–4122. https://doi.org/10.1118/1.4725171
22. Urikura A, Ichikawa K, Hara T, Nishimaru E, Nakaya Y (2014) Spatial resolution measurement for iterative reconstruction by use of image-averaging techniques in computed tomography. Radiol Phys Technol 7:358–366. https://doi.org/10.1007/s12194-014-0273-2
23. Ichikawa K CT measure: Japanese Society of CT Technology; [Available from: https://www.jsct-tech.org/en/]. Accessed 2 Aug 2023
24. Samei E, Bakalyar D, Boedeker KL, Brady S, Fan J, Leng S et al (2019) Performance evaluation of computed tomography systems: summary of AAPM Task Group 233. Med Phys 46:e735–e756. https://doi.org/10.1002/mp.13763
25. Urikura A, Hara T, Ichikawa K, Nishimaru E, Hoshino T, Yoshida T et al (2016) Objective assessment of low-contrast computed tomography images with iterative reconstruction. Phys Med 32:992–998. https://doi.org/10.1016/j.ejmp.2016.07.003
26. Hasegawa A, Ichikawa K, Morioka Y, Kawashima H (2022) A tin filter's dose reduction effect revisited: using the detectability index in low-dose computed tomography for the chest. Phys Med 99:61–67. https://doi.org/10.1016/j.ejmp.2022.05.006
27. Higaki T, Nakamura Y, Zhou J, Yu Z, Nemoto T, Tatsugami F et al (2020) Deep learning reconstruction at CT: phantom study of the image characteristics. Acad Radiol 27:82–87. https://doi.org/10.1016/j.acra.2019.09.008
28. Racine D, Becce F, Viry A, Monnin P, Thomsen B, Verdun FR et al (2020) Task-based characterization of a deep learning image reconstruction and comparison with filtered back-projection and a partial model-based iterative reconstruction in abdominal CT: a phantom study. Phys Med 76:28–37. https://doi.org/10.1016/j.ejmp.2020.06.004
29. Nagayama Y, Oda S, Nakaura T, Tsuji A, Urata J, Furusawa M et al (2018) Radiation dose reduction at pediatric CT: use of low tube voltage and iterative reconstruction. Radiographics 38:1421–1440. https://doi.org/10.1148/rg.2018180041